

Gravitational Instability of Shocked Interstellar Gas Layers

Kazunari IWASAKI and Toru TSURIBE

*Department of Earth and Space Science, Osaka University, Machikaneyama 1-1 Toyonaka 560-0043, Osaka
iwasaki@vega.ess.sci.osaka-u.ac.jp, tsuribe@vega.ess.sci.osaka-u.ac.jp*

(Received (reception date); accepted (acceptation date))

Abstract

In this paper we investigate gravitational instability of shocked gas layers using linear analysis. An unperturbed state is a self-gravitating isothermal layer which grows with time by the accretion of gas through shock fronts due to a cloud-cloud collision. Since the unperturbed state is not static, and cannot be described by a self-similar solution, we numerically solved the perturbation equations and directly integrated them over time. We took account of the distribution of physical quantities across the thickness. Linearized Rankine-Hugoniot relations were imposed at shock fronts as boundary conditions. The following results are found from our unsteady linear analysis: the perturbation initially evolves in oscillatory mode, and begins to grow at a certain epoch. The wavenumber of the fastest growing mode is given by $k = 2\sqrt{2\pi G\rho_E\mathcal{M}}/c_s$, where ρ_E , c_s and \mathcal{M} are the density of parent clouds, the sound velocity and the Mach number of the collision velocity, respectively. For this mode, the transition epoch from oscillatory to growing mode is given by $t_g = 1.2/\sqrt{2\pi G\rho_E\mathcal{M}}$. The epoch at which the fastest growing mode becomes non-linear is given by $2.4\delta_0^{-0.1}/\sqrt{2\pi G\rho_E\mathcal{M}}$, where δ_0 is the initial amplitude of the perturbation of the column density. As an application of our linear analysis, we investigate criteria for collision-induced fragmentation. Collision-induced fragmentation will occur only when parent clouds are cold, or $\alpha_0 = 5c_s^2 R/2GM < 1$, where R and M are the radius and the mass of parent clouds, respectively.

Key words: Hydrodynamics — Instability — Interstellar: clouds — Stars: formation

1. Introduction

Shock waves that propagate in interstellar gases play important roles in the formation of stars and other structures in the universe. Shock waves are formed by cloud-cloud collisions (Hasegawa et al. 1994, Sato et al. 2000), supernova explosions (Herbst & Assousa 1977), expansions of HII regions by ionizing photons emitted from OB stars (Blaauw 1964), and so on. Shock waves sweep out external gases and form highly compressed sheet-like structures behind the shock fronts. These layers, which are sheet-like structures, are often supposed to fragment and eventually to form stars.

Shock compression contributes especially on the formation of aggregations of stars. Elmegreen & Lada (1977) proposed a scenario of a sequential formation of OB star subgroups. The expansion of a HII region that is formed by an OB subgroup sweeps up the gases. A highly compressed layer forms, and then possibly fragments. Thereafter, a new OB star subgroup forms from the layer, and the ionizing photons emitted from the new subgroup induce the formation of next subgroup by the same process. Kumai et al. (1993) proposed a scenario of a globular cluster formation that is induced by the gravitational instability of a layer formed by a supersonic collision between large proto-globular cluster clouds. Observations showed that galaxies containing young star clusters have larger random velocity dispersions of gases than those that do not have young clusters (Fujimoto & Noguchi 1990). If the large random velocity dispersion of gases is stimulated

by mergers or interactions between galaxies (Ashman & Zepf 1992), the scenario of star cluster formation by cloud-cloud collision is indicated.

In the process of star cluster formation from the layer, it is crucial to understand when and how a shock-compressed layer fragments. Goldreich & Lynden-Bell (1965) (hereafter GL65) and Elmegreen & Elmegreen (1978) investigated the stability of a static isothermal self-gravitating layer that is supported by constant external pressure on both sides using linear analysis. They showed that the wave length of the most unstable mode is approximately the scale height of gravity, $H_0 = c_s/\sqrt{2\pi G\rho_{00}}$ when the density at the central plane, ρ_{00} , is larger than the boundaries, ρ_b , of the layer ($\rho_{00}/\rho_b > 1$). When $\rho_{00}/\rho_b \simeq 1$, the wave length of the most unstable mode is the thickness of the layer. The maximum growth rate is about the free-fall growth rate of the layer in both cases.

However, a layer formed by shock compression is bounded by shock waves on at least one side. The effects of the shock boundary strongly influence the stability of the layer when $\rho_{00}/\rho_b \simeq 1$. This is because the layer is mainly confined not by self-gravity, but by external pressure. Vishniac (1994) (hereafter V94) derived a simple dispersion relation of a layer bounded by shocks on both sides using shock boundary conditions, while neglecting the time dependence of the column density. The dispersion relation of the shocked layer is quite different from that of the static layer when $\rho_{00}/\rho_b \simeq 1$ (see Appendix 2 and 3). Therefore, the results with a constant pressure boundary are not applicable to a layer bounded by a shock

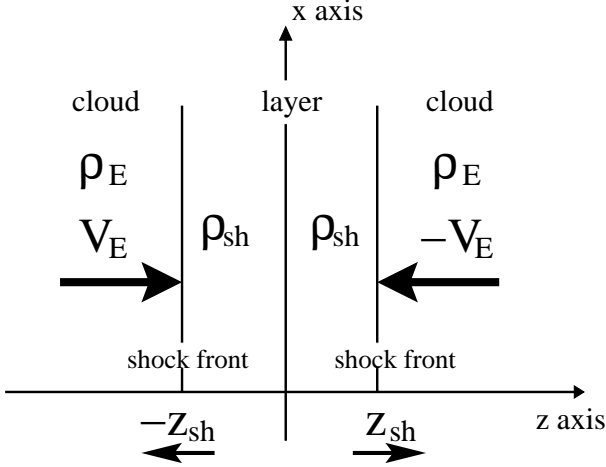


Fig. 1. Schematic picture of a compressed layer between the shock fronts.

front when $\rho_{00}/\rho_b \simeq 1$. Since the layer experiences the state of $\rho_{00}/\rho_b \simeq 1$ in early phase from the moment when the layer is formed by collision, an analysis that takes account of the effect of the shock boundary is important.

In the analysis of V94, the time evolution of the column density is not considered. In this paper, in order to consider the fastest growing mode in the layer that is formed by cloud-cloud collision, we take into account both shock boundary and time-dependent column density. The distribution of the physical variables across the thickness is also taken into account accurately.

In section 2, we set up a model of a layer. Before our linear analysis, previous works (V94; Whitworth et al. 1994) using a 1-zone model is reviewed. In section 3, an unperturbed state is described. In section 4, perturbation equations are derived and a numerical method, boundary conditions and initial conditions are shown. The results are shown in section 5. Criteria for collision-induced fragmentation are discussed in section 6. Our study is summarized in section 7.

2. Model

2.1. Assumptions

We consider a head-on collision of two physically identical clouds with sufficiently large Mach number ($\mathcal{M} \gg 1$). The equation of state is assumed to be isothermal. In this paper, Cartesian coordinates (x, y, z) are used and the z -axis is perpendicular to a layer. The layer is assumed to extend infinitely in the x - y plane. We can discuss the system in the x - z plane without any loss of generality in the linear regime. Physically identical clouds are assumed to collide along the z -axis with velocity $\pm V_E$ and density ρ_E at $t = 0$ and $z = 0$. The two shock fronts at $z = \pm z_{sh}$ propagate in both directions and a highly compressed layer is formed between two shock fronts (see figure 1). The isothermal shock boundary conditions are given by

$$\rho_{sh} = \rho_E \mathcal{M}^2, \quad z_{sh} = \frac{c_s}{\mathcal{M}}, \quad \text{and} \quad V_E = \left(\mathcal{M} - \frac{1}{\mathcal{M}} \right) c_s, \quad (1)$$

where $\mathcal{M} = V_{sh}/c_s$ is the Mach number and V_{sh} is the velocity of the clouds in the rest frame of the shock front (see Appendix 1 in detail). The unperturbed column density, Σ_0 , is defined by

$$\Sigma_0(t) = \int_{-z_{sh}}^{z_{sh}} \rho_0(z) dz = 2\rho_E \mathcal{M} c_s t, \quad (2)$$

which increases as $\propto t$ by gas accretion. Hereafter, we investigate gravitational instability of the layer between two shock fronts.

2.2. Dispersion Relation under 1-zone Model

As an essential guide for our linear analysis, a simple dispersion relation using a 1-zone model is summarized (see V94 in detail). In the 1-zone model, we consider averaged physical quantities across the thickness. The layer is assumed to be geometrically thin, i.e., $z_{sh}/H_0 \ll 1$ and $kL_0 \ll 1$, where L_0 and $H_0 = c_s/\sqrt{2\pi G\rho_{sh}}$ are the thickness and the scale height of the layer, respectively. Averaging physical variables across the thickness and neglecting the time evolution of $\Sigma_0(t)$ with shock boundary condition, V94 derived an approximate dispersion relation which is given by

$$\omega^2 \sim c_s^2 k^2 - 2\pi G k \Sigma_0(t). \quad (3)$$

The derivation of equation (3) is shown in Appendix 2. The dispersion relation is identical to that of an infinitely thin disk without boundary condition. In Appendix 3, we derive a dispersion relation of a static layer which is confined by constant external pressure by the using 1-zone model for comparison.

According to equation (3), the time evolution of the perturbations with wavenumber k is described as follows: in the early phase $t \sim 0$, the equation (3) is approximately $\omega^2 \sim c_s^2 k^2$, because $\Sigma_0(t)$ is small. Thus, the perturbations are initially in an oscillatory mode. Since $c_s^2 k^2$ is constant with time, while $2\pi G k \Sigma_0(t)$ increases with time, the perturbations will change from the oscillatory mode to a growing mode at a certain epoch.

This transition epoch can be derived by a simple order estimation. The gravitational instability sets in if $\sqrt{-\omega^2} > 1/t$ (Whitworth et al. 1994), where $1/t$ is the evolution rate of the unperturbed layer by gas accretion. The transition epoch, $t_{c,k}$, at which perturbations with wavenumber k begin to grow, is given by

$$\frac{1}{t_{c,k}} = \sqrt{-\omega^2} = \sqrt{2\pi G k \Sigma_0(t_{c,k}) - c_s^2 k^2}. \quad (4)$$

Using the characteristic timescale and the wavenumber defined by

$$t_c = 1/\sqrt{2\pi G \rho_E \mathcal{M}} \quad \text{and} \quad k_c = \sqrt{2\pi G \rho_E \mathcal{M}}/c_s, \quad (5)$$

equation (4) is rewritten as an independent form on Mach number as

$$\frac{1}{\tilde{\tau}_{c,\kappa}} = \sqrt{2\tilde{\tau}_{c,\kappa} \kappa - \kappa^2}, \quad (6)$$

where $\tilde{\tau} = t/t_c$ and $\kappa = k/k_c$. Figure 2a shows the dependence of $\tilde{\tau}_{c,\kappa}$ on the wavenumber κ . Figure 2a indicates

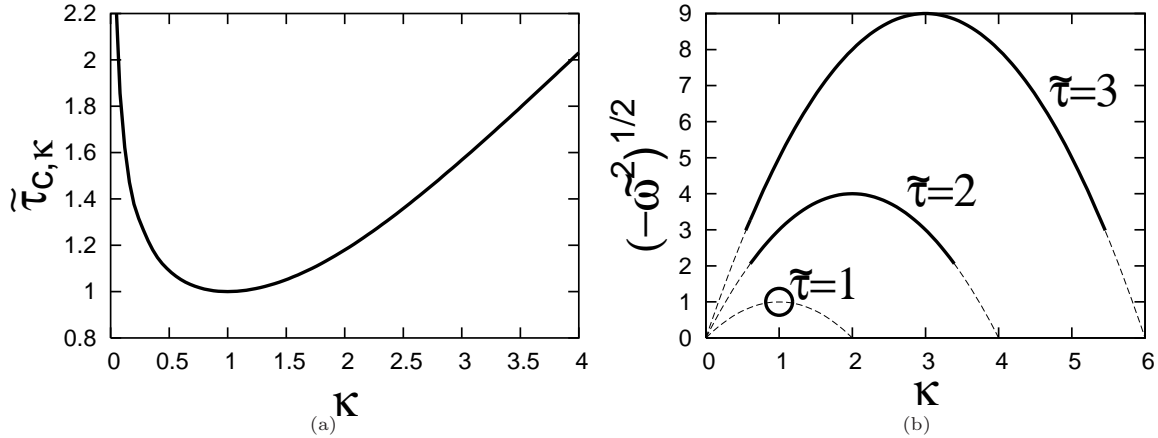


Fig. 2. (a) Dependence of the transition epoch, $\tilde{\tau}_{C,\kappa}$, from oscillatory to growing mode on wavenumbers κ in the 1-zone model. The curve shows a plot of equation (6). (b) Dispersion relation [equation (3)] at $\tilde{\tau}=1, 2$ and 3 , where $\tilde{\omega} = t_c \omega$. The solid lines satisfy $\sqrt{-\tilde{\omega}^2} > 1/t$, where perturbation grows faster than growth of the column density. The open circle indicates the mode that begins to grow at the earliest epoch, $\kappa = 1$.

that the mode with $\kappa = 1$ begins to grow at the earliest epoch $\tilde{\tau} = 1$. Then, the perturbations with $\kappa \sim 1$ switch to the gravitational instability successively. Whitworth et al. (1994) estimated fragmentation mass scale using $\kappa = 1$. However, the earliest transition mode, $\kappa = 1$, is not the fastest growing mode in later epoch. Figure 2b represents the dispersion relation [equation (3)] at $\tilde{\tau}=1, 2$ and 3 , where $\tilde{\omega} = t_c \omega$. The open circle indicates the earliest transition mode, $\kappa = 1$. The gravitationally unstable state that satisfies $\sqrt{-\tilde{\omega}^2} > 1/t$ is shown by the solid lines at each epoch. Figure 2b indicates that $\tilde{\omega}$ and κ of the fastest growing mode varies with time.

In the discussions so far, have been based on equation (3), which was derived by neglecting the time dependence of $\Sigma_0(t)$. However, especially during $t \lesssim t_{c,k}$, the evolution rate of the layer $1/t$ is larger than $\sqrt{-\tilde{\omega}^2}$. Therefore, the evolution of $\Sigma_0(t)$ can not be neglected. In this paper, in order to accurately predict the fragmentation scale of the evolving layer at the earliest epoch, the evolution of the unperturbed layer is taken into account consistently. In the following sections, we investigate the gravitational instability in the linear regime with a time-dependent $\Sigma_0(t)$, as well as shock boundary conditions without the 1-zone approximation.

3. Unperturbed State

In our linear analysis, the unperturbed state is the time-evolving layer formed by cloud collision. To begin with, we define the distribution of the density, $\rho(z, t)$. The density distribution of a hydrostatic isothermal self-gravitating layer that is supported by external pressure, P_b , is analytically written as

$$\rho(z) = \frac{\rho_{00}}{\cosh^2(z/H_0)}, \quad H_0 = \frac{c_s}{\sqrt{2\pi G \rho_{00}}}. \quad (7)$$

The relationship among ρ_{00} , P_b and Σ_0 is given by

$$\rho_{00} = \frac{P_b}{c_s^2} + \frac{\pi G \Sigma_0^2}{2c_s^2}. \quad (8)$$

Equation (8) shows that a set of external pressure P_b and the column density Σ_0 provides a unique density distribution $\rho(z)$.

The sound-crossing time across the thickness L_0 and evolution time are defined by $t_{\text{cross}} = L_0/c_s$ and $t_{\text{evo}} = \Sigma_0/(d\Sigma/dt) = t$, respectively. Since the thickness L_0 varies as $\lesssim 2c_s t/\mathcal{M}$, the ratio between the two timescales is $t_{\text{cross}}/t_{\text{evo}} \lesssim 2/\mathcal{M} \ll 1$. Therefore, we assume that the layer evolves while maintaining the equilibrium density distribution in the z -direction with a large Mach number.

Next, we assume that the Mach number, \mathcal{M} at the shock front is constant. We consider the evolution of the shock front in the rest frame of the $z=0$ plane. According to equation (1), if V_E is constant, the shock front velocity, \dot{z}_{sh} , is constant without gravity. If gravity is taken into account, as the effect of gravity becomes important, \dot{z}_{sh} decreases with time. Consequently, in the rest frame of shock front, the velocity of accreting gas, $V_{\text{sh}} = V_E + \dot{z}_{\text{sh}}$, and the Mach number \mathcal{M} decrease. However the fractional change of Mach number is as small as $\mathcal{M}^{-2} \ll 1$. Therefore, the constant \mathcal{M} assumption well approximates a constant V_E .

The velocity distribution in the postshock layer is assumed to be zero. In reality, $v_z(z, t)$ is not zero in order to attain the hydrostatic state at each instant of time. However, this assumption is also valid when the Mach number is sufficiently large. The validity of this assumption is discussed in Appendix 4.

The above assumptions completely provide the time evolution of the density distribution and the position of the shock front analytically. With a constant Mach number, the column density and the external pressure are given by

$$\Sigma_0(t) = 2\rho_E \mathcal{M} c_s t, \quad P_b = c_s^2 \rho_E \mathcal{M}^2. \quad (9)$$

Substituting equation (9) into equation (8), the density at the center is obtained as

$$\rho_{00} = \rho_E \mathcal{M}^2 (1 + \tau^2), \quad (10)$$

where τ is defined by $\tau = t\sqrt{2\pi G\rho_E}$, which is the time normalized by the free-fall timescale in the preshock region. Equation (10) shows that the layer has approximately uniform density distribution, $\rho_{00}/\rho_b \sim 1$, at $\tau \ll 1$, and $\rho_{00}/\rho_b = 2$ at $\tau = 1$. Because the density at the shock front is given by $\rho_E \mathcal{M}^2$, the time evolution of $z_{\text{sh}}(t)$ is written with equation (7) as

$$\begin{aligned} z_{\text{sh}} &= H_0 \cosh^{-1} \sqrt{1 + \tau^2} \\ &= \frac{c_s}{\mathcal{M}} \frac{1}{\sqrt{2\pi G\rho_E}} \frac{\cosh^{-1} \sqrt{1 + \tau^2}}{\sqrt{1 + \tau^2}}. \end{aligned} \quad (11)$$

When $\tau \ll 1$, equation (11) becomes $z_{\text{sh}} \sim c_s t / \mathcal{M}$. As τ increases, the increasing rate of z_{sh} is suppressed by self-gravity. At $\tau \sim 1.5$, z_{sh} reaches the maximum and begins to decrease.

4. Perturbed State

In this section, we consider perturbations on the unperturbed state, which is defined in the previous section. To begin, the basic equations of ideal self-gravitating isothermal fluid are the mass conservation,

$$\frac{\partial \rho}{\partial t} + \nabla \cdot (\rho \mathbf{v}) = 0, \quad (12)$$

the momentum conservation,

$$\frac{\partial}{\partial t} (\rho \mathbf{v}) + \nabla \cdot (\rho \mathbf{v} \otimes \mathbf{v} + P \mathbf{I}) + \rho \nabla \phi = 0, \quad (13)$$

the Poisson equation,

$$\nabla^2 \phi = 4\pi G \rho, \quad (14)$$

and isothermal condition,

$$\frac{P}{\rho} = c_s^2 = \text{const}, \quad (15)$$

where \mathbf{I} is the unit matrix and ϕ is the gravitational potential. The perturbation variables ($\delta\rho$, δv_z , δv_x and $\delta\phi$) are defined by

$$\rho(x, z, t) = \rho_0(z, t) + \delta\rho(z, t)e^{ikx}, \quad (16)$$

$$v_z(x, z, t) = v_{z,0}(z, t) + \delta v_z(z, t)e^{ikx}, \quad (17)$$

$$v_x(x, z, t) = \delta v_x(z, t)e^{ikx}, \quad (18)$$

and

$$\phi(x, z, t) = \phi_0(z, t) + \delta\phi(z, t)e^{ikx}, \quad (19)$$

where we take the Fourier mode in the x -direction. Subscript "0" denotes quantities of the unperturbed state. By linearizing the basic equations about the perturbation variables, the perturbation equations are given by

$$\frac{\partial \delta\rho}{\partial t} + \frac{\partial}{\partial z} (\rho_0 \delta v_z) = -ik\rho_0 \delta v_x, \quad (20)$$

$$\frac{\partial}{\partial t} (\rho_0 \delta v_z) + \frac{\partial}{\partial z} (c_s^2 \delta\rho) = -\delta\rho \frac{\partial \phi_0}{\partial z} - \rho_0 \frac{\partial \delta\phi}{\partial z}, \quad (21)$$

$$\frac{\partial}{\partial t} (\rho_0 \delta v_x) = -ikc_s^2 \delta\rho - ik\rho_0 \delta\phi, \quad (22)$$

and

$$\frac{\partial^2 \delta\phi}{\partial z^2} - k^2 \delta\phi = 4\pi G \delta\rho, \quad (23)$$

where we assume $v_{z,0} = 0$.

The rippling of the shock front δz_{sh} is defined by

$$z_{\text{sh}}(x, t) = z_{\text{sh},0}(t) + \delta z_{\text{sh}}(t)e^{ikx}. \quad (24)$$

The column density perturbation, which is defined by

$$\delta\Sigma = \int_{-z_{\text{sh}}}^{z_{\text{sh}}} \rho(x, z, t) dz - \Sigma_0, \quad (25)$$

can be divided into two contributions, as follows:

$$\delta\Sigma = \rho_{\text{sh}} \delta L + \delta\sigma, \quad (26)$$

where $\delta L = 2\delta z_{\text{sh}}$ and $\delta\sigma = \int_{-z_{\text{sh},0}}^{z_{\text{sh},0}} \delta\rho dz$. The first term describes the fluctuation of the shock boundary, and the second term describes the contribution of density perturbation inside the layer.

Since the unperturbed state is neither static nor self-similar solution, the perturbation equations are not reduced to some eigenvalue problems. Therefore, we directly integrate the perturbation equations over both time and the z -direction to investigate the time evolution of the perturbations.

4.1. Numerical Method

The upwind finite-difference method is used as numerical scheme. Because the perturbation equations have source terms, the numerical flux is modified appropriately (Hubbard & Garcia-Navarro 2000).

We performed three tests of our code. First, we calculated $k = 0$ perturbation without self-gravity. The results of our calculation were compared to the results of a one-dimensional, non-linear hydrodynamical calculation using 2nd-order Godunov code in the same situation. Our linear results agree with the non-linear calculation very well. Secondly, we calculated the case with $k \neq 0$ without self-gravity. V94 derived the dispersion relation of the even mode to be $\omega = \pm c_s k (1 - 2/\mathcal{M}^2)$. We obtained the same frequency as V94. Thirdly, we calculated stability of the static self-gravitating layer. Our results agree with the growth rate of GL65. In these test calculations, our code provided correct results.

4.2. Boundary Conditions

The boundary conditions are set at $z = 0$ and $z = z_{\text{sh},0}$. We investigate the even mode, and the boundary conditions at $z = 0$ are given by

$$\left(\frac{\partial \delta\rho}{\partial z} \right)_{z=0} = 0, \quad \left(\frac{\partial \delta\phi}{\partial z} \right)_{z=0} = 0, \quad \text{and} \quad \delta v_z(z=0) = 0. \quad (27)$$

At the shock front $z_{\text{sh},0}$, the physical variables must satisfy the Rankine-Hugoniot relations. Thus, we impose linearized Rankine-Hugoniot relations at $z_{\text{sh},0}$ (see Appendix 1 in detail), which are given by

$$\delta\rho_{\text{sh}} = -\delta z_{\text{sh}} \left(\frac{\partial\rho_0}{\partial z} \right)_{z=z_{\text{sh},0}} + 2\rho_{\text{E}} \frac{\mathcal{M}}{c_s} \frac{d\delta z_{\text{sh}}}{dt}, \quad (28)$$

$$\delta v_{z,\text{sh}} = -\delta z_{\text{sh}} \left(\frac{\partial v_z}{\partial z} \right)_{z=z_{\text{sh},0}} + \left(1 + \frac{1}{\mathcal{M}^2} \right) \frac{d\delta z_{\text{sh}}}{dt}, \quad (29)$$

$$\delta v_{x,\text{sh}} = -ikV_{\text{E}}\delta z_{\text{sh}} \quad (30)$$

and

$$\frac{\partial\delta\phi_{\text{sh}}}{\partial z} + k\delta\phi_{\text{sh}} + 4\pi G(\rho_{\text{sh}} - \rho_{\text{E}})\delta z_{\text{sh}} = 0, \quad (31)$$

where subscript "sh" indicates the value at the shock front.

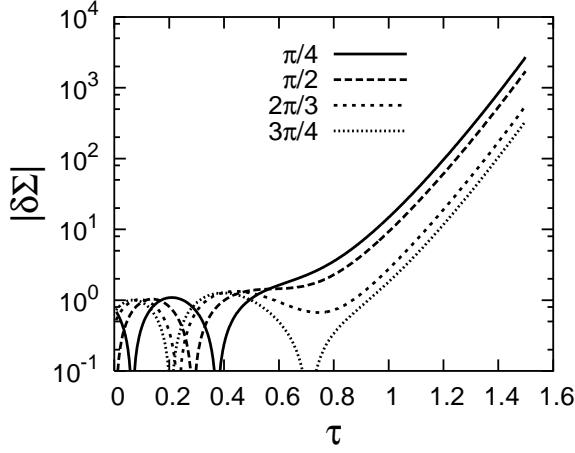


Fig. 3. Time evolution of $\delta\Sigma$ for $\kappa = 4$ and $\mathcal{M} = 10$. Each line corresponds to initial phases $\psi = \pi/4, \pi/2, 2\pi/3, 3\pi/4$, respectively.

4.3. Initial Conditions

The initial epoch is set to be $\tau_{\text{ini}} = 5 \times 10^{-3}$, but the results are not sensitive to τ_{ini} as long as it is sufficiently small. As an initial condition, an oscillatory mode (see subsection 2.2) without self-gravity is adopted. The time evolution of perturbations depends on an initial phase ψ of perturbation in oscillatory mode. In figure 3, the evolution of $\delta\Sigma$ with different initial phases is shown for $\mathcal{M}=10$ and $\kappa = 4$. In this paper, we focus on the evolution with the initial phase by which $\delta\Sigma$ grows fastest.

5. Results

5.1. The Evolution of Perturbations

Figure 4 shows the time evolution of $\delta\Sigma$ for various Mach numbers, ($\mathcal{M} = 10, 30, 50$ and 100). Figures 4a and 4b correspond to $\kappa = 1$ and 2 , respectively. The thin dot-dashed line shows the result without self-gravity for $\mathcal{M} = 10$. The thick solid line shows the result with self-gravity for $\mathcal{M}=10$. In both of figures 4a and 4b, the lines for $\mathcal{M} = 10$ with and without self-gravity are identical initially ($\tau \lesssim 0.1$). Later, the thick solid line with self-gravity changes to a growing mode at $\tau \sim 0.2 - 0.3$. We define the

epoch of transition from an oscillatory mode to a growing mode as τ_{g} , which corresponds to the inflection point of $\delta\Sigma$ ($d^2\delta\Sigma/d\tau^2 = 0$). We will find that τ_{g} is well approximated by $t_{c,k}$ in the 1-zone model in subsection 2.2. In figures 4a and 4b, it is also seen that the growth rate is larger and τ_{g} is smaller for the larger Mach number. The dependences of the growth rate and τ_{g} on the Mach number are discussed quantitatively in subsection 5.2.

As shown in equation (26), $\delta\Sigma$ consists of $\rho_{\text{sh}}\delta L$ and $\delta\sigma$. In figure 5, it can be clearly seen that the fluctuation of the boundary $\rho_{\text{sh}}\delta L$ dominates in the evolution of the perturbations during $\tau \lesssim 1$. On the other hand, $\delta\sigma$ stays much smaller than $\rho_{\text{sh}}\delta L$ in $\tau \lesssim 1$. This means that the layer behaves like an incompressible fluid for $\tau \lesssim 1$. For this reason, as an indicator of the perturbation amplitude, we mainly use the column density perturbation, $\delta\Sigma$, instead of $\delta\rho(z)$.

Figure 6 shows the density perturbation, $\delta\rho(z)$, inside the layer at various epochs, $\tau = 0.2, 0.4, 0.6$ and 1.0 for $\mathcal{M} = 10$ and $\kappa = 1$. As normalization, we set $\delta z_{\text{sh}}/z_{\text{sh},0} = 0.05$ at $\tau = 0.6$. The abscissa and the ordinate axes are normalized by $z_0 = c_s/(\sqrt{2\pi G\rho_{\text{E}}}\mathcal{M})$ and $\rho_{\text{sh}} = \mathcal{M}^2\rho_{\text{E}}$, respectively. The position of the shock front, $z_{\text{sh},0}$, is seen as the right edge of each line. At $\tau \gtrsim 0.3$ the perturbations become gravitationally unstable (c.f., figure 4a), and $\delta\rho$ increases with time.

Figure 7 shows cross sections of the perturbed layer at (a) $\tau = 0.6$ and (b) $\tau = 1.0$. The normalization of the perturbation is the same as in figure 6. It can be seen that the perturbation grows gravitationally from $\tau = 0.6$ to 1.0 . Near the equatorial plane, inflow in the x -direction is generated by gravity, which reflects to enhancing the shock front. In contrast, near the shock boundary, the perturbed velocity field is outward in the x -direction. This tangential flow is the result of the shock boundary condition. This momentum flow acts against the force of gravity (see Appendix 2.2 in detail).

5.2. The Growth Rate and Transition Epoch

We discuss the dependence of the growth rate and the transition epoch, τ_{g} , on Mach number. In the 1-zone model, according to equation (5), the dependence of the transition epoch, $\tau_{c,\kappa}$, on Mach number is $\mathcal{M}^{-1/2}$. To see whether the same scaling relation holds or not in the model without the 1-zone approximation, we replot figure 4 in figure 8 using $\tilde{\tau} = \tau\mathcal{M}^{1/2}$ as the abscissa.

In figures 8a and 8b, it is seen that each line for different Mach numbers is nearly identical. This result is explained as follows: in the 1-zone model, from equation (3), the time evolution of $\delta\Sigma$ is expressed as

$$\frac{\partial \ln \delta\Sigma}{\partial t} = \sqrt{-\omega^2} \rightarrow \frac{\partial \ln \delta\Sigma}{\partial \tilde{\tau}} = \sqrt{2\kappa\tilde{\tau} - \kappa^2}, \quad (32)$$

where $\tilde{\tau} = \sqrt{\mathcal{M}}\tau$. Integrating this equation over $\tilde{\tau}$, we obtain

$$\delta\Sigma \propto \exp \left[\frac{1}{3\kappa} (2\kappa\tilde{\tau} - \kappa^2)^{3/2} \right]. \quad (33)$$

Equation (33) shows that the time evolution of $\delta\Sigma$ seems

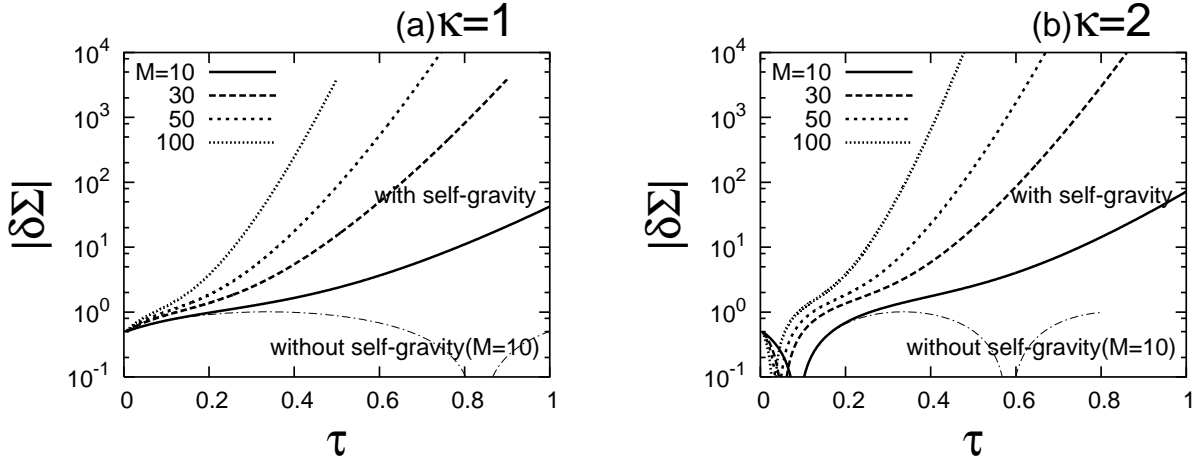


Fig. 4. Time evolution of $\delta\Sigma$ for the case with (a) $\kappa = 1$ and (b) $\kappa = 2$. In each panel, thick lines correspond to the case with self-gravity ($\mathcal{M}=10, 30, 50$ and 100), while the thin dot-dashed line corresponds to the case without self-gravity ($\mathcal{M} = 10$).

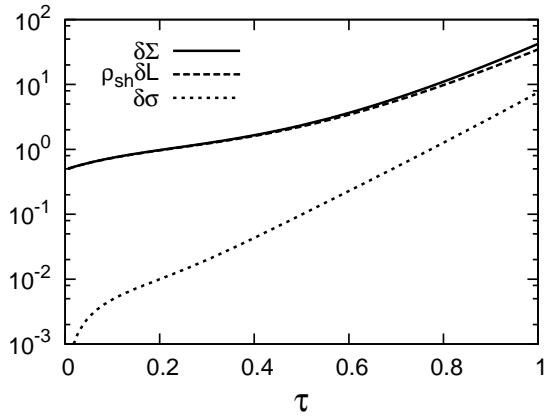


Fig. 5. Time evolution of $\delta\Sigma$ (solid line), $\rho_{\text{sh}}\delta L$ (long-dashed line) and $\delta\sigma$ (short-dashed line) for $\mathcal{M}=10$ and $\kappa = 1$.

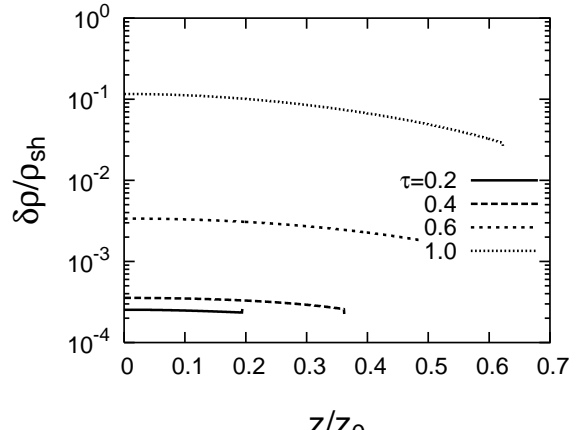


Fig. 6. Distributions of density perturbation $\delta\rho(z)$ at $\tau = 0.2, 0.4, 0.6$ and 1.0 . The abscissa is normalized by $z_0 = c_s/(\sqrt{2\pi G\rho_E\mathcal{M}})$. The ordinate is normalized by $\rho_E\mathcal{M}^2$.

to be independent of the Mach number if we take $\tilde{\tau}$ as dimensionless time. Therefore, the growth rate of our calculation is also expected to be independent of the Mach number using the normalized time, t/t_c , and the wavenumber, k/k_c .

Next, we consider the transition epoch from an oscillatory to a growing mode. In figure 8, it is clearly seen that $\delta\Sigma$ changes from the oscillatory to the growing mode at the same value of $\tau\mathcal{M}^{1/2}$. The filled circle indicates the transition epoch $\tilde{\tau}_{c,\kappa}$ predicted from the 1-zone model. In both of figures 8 (a) $\kappa = 1$ and (b) $\kappa = 2$, it is seen that $\delta\Sigma$ begins to grow at $\tau_g\mathcal{M}^{1/2} = \tilde{\tau}_{c,\kappa}$, where τ_g corresponds to the inflection point of $\delta\Sigma$. We checked that $\tau_{c,\kappa}$ in the 1-zone model gives a correct transition epoch even in the model without the 1-zone approximation, at least for $0.125 \leq \kappa \leq 8$.

5.3. Time-Evolving Dispersion Relations

Dispersion relations at each instant of time are considered. The growth rate at t is defined by

$$\omega \equiv \frac{d}{dt} \left\{ \ln \left(\frac{\delta\Sigma}{\Sigma_0} \right) \right\}. \quad (34)$$

Figure 9a shows the dispersion relation derived from equation (34) at each instant of time for $\mathcal{M} = 30$. Figure 9b shows dispersion relations for a static layer corresponding to the density distribution at each instant of time (see GL65). When $\tau < 1$, the distinction between figure 9a and figure 9b is obvious. In the static layer, when $\tau \rightarrow 0$, $(\sqrt{-\omega^2})_{\text{max}}$ and k_{max}^{-1} are given by the free-fall growth rate and the thickness of the layer, respectively (see Appendix 3). However, in the shocked layer, $(\sqrt{-\omega^2})_{\text{max}}$ and k_{max} converge to the zero as $\tau \rightarrow 0$. Thus, imposing shock boundary condition is important to understand the fragmentation process in the shocked layer. Welter (1982) reported a similar property for a layer with shock on one side.

5.4. Fragmentation Time: When Perturbation Becomes Non-linear

Since the growth rate depends on both the time and the wavenumber (figure 9a, figure 2b), the above discussion is

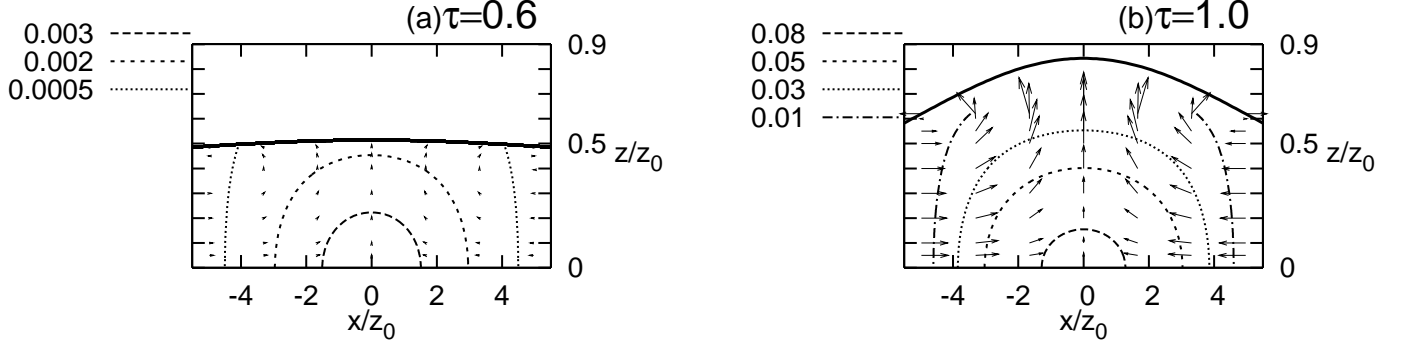


Fig. 7. Cross sections of the perturbed layer for $\mathcal{M}=10$ and $\kappa=2$ at (a) $\tau=0.6$ and (b) $\tau=1.0$. The normalization $\delta z_{\text{sh}}/z_{\text{sh},0}=0.05$ at $\tau=0.6$ is used. Contours denote the density perturbation normalized by $\rho_E \mathcal{M}^2$, and arrows denote the velocity perturbation fields of which length represents their magnitude. The thick solid lines show $z_{\text{sh}} = z_{\text{sh},0} + \delta z_{\text{sh}}$. The abscissa and the ordinate are normalized by z_0 as figure 6. The unperturbed shock position at $\tau=0.6$ and 1.0 are $z_{\text{sh},0}=0.49z_0$ and $0.62z_0$, respectively.

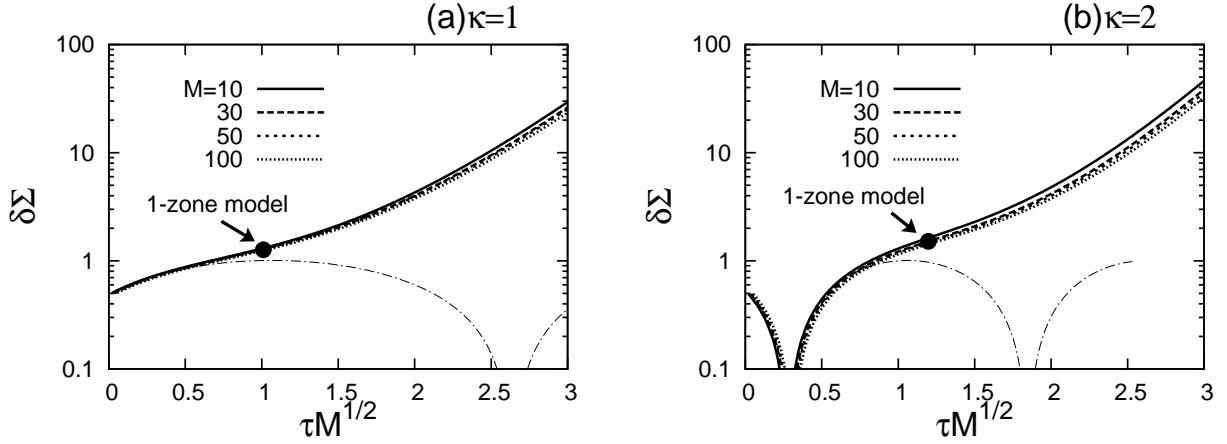


Fig. 8. The same figure as the figure 4 except that the abscissa denotes normalized time $\hat{\tau} = \tau \mathcal{M}$ which is defined in subsection 2.2. Filled circle shows the transition time $\hat{\tau}_{c,\kappa}$ which is predicted from 1-zone model in subsection 2.2.

not sufficient to predict the fragmentation scale. Thus, we consider the wavenumber that becomes non-linear at the earliest epoch. The time τ_{nl} when a mode becomes non-linear is defined by

$$\frac{\delta \Sigma(\tau_{\text{nl}})}{\Sigma_0(\tau_{\text{nl}})} \equiv 1. \quad (35)$$

The time τ_{nl} depends on the wavenumber and the initial amplitude of the perturbation. To focus on the evolution after the transition epoch, $\tau_{c,\kappa}$, we define the initial amplitude δ_0 at $\tau_{c,\kappa}$, by

$$\frac{\delta \Sigma(\tau_{c,\kappa})}{\Sigma_0(\tau_{c,\kappa})} \equiv \delta_0. \quad (36)$$

Combining this definition with $\Sigma_0 \propto t$, we obtain

$$\delta_0 \frac{\delta \Sigma(\tau_{\text{nl}})}{\delta \Sigma(\tau_{c,\kappa})} \frac{\tau_{c,\kappa}}{\tau_{\text{nl}}} = 1. \quad (37)$$

The arrival time τ_{nl} , which satisfies equation (37), is calculated as a result of our linear analysis.

5.5. The Fastest Growing mode

In this section, we determine the wavenumber that becomes non-linear at the earliest epoch by using equation (37). Figure 10 represents the dependence of τ_{nl} on the wavenumber for various \mathcal{M} and initial amplitude, δ_0 . Figure 10 shows that the mode with $\kappa=2$ becomes non-linear at the earliest epoch for all \mathcal{M} and δ_0 . Note that this wavenumber is different from one ($\kappa=1$, figure 2), which becomes unstable at the earliest epoch (see subsection 2.2). For the fastest growing mode, $\kappa_{\text{nl}}=2$, the dependence of τ_{nl} on the Mach numbers is shown in figure 11. From figure 11, we can see that $\tau_{\text{nl}} \propto \mathcal{M}^{-1/2}$ holds for each δ_0 . This Mach number dependence is simply understood by the fact that equation (33) does not contain \mathcal{M} with normalized t/t_c and k/k_c . By fitting the dependence on δ_0 , τ_{nl} is finally given by

$$\tau_{\text{nl}} \sim 2.4 \delta_0^{-0.1} \mathcal{M}^{-1/2}. \quad (38)$$

The error of this fitting formulae is less than 10% for $10^{-3} < \delta_0 < 0.1$.

Since the dependence on δ_0 is small in equation (38), if

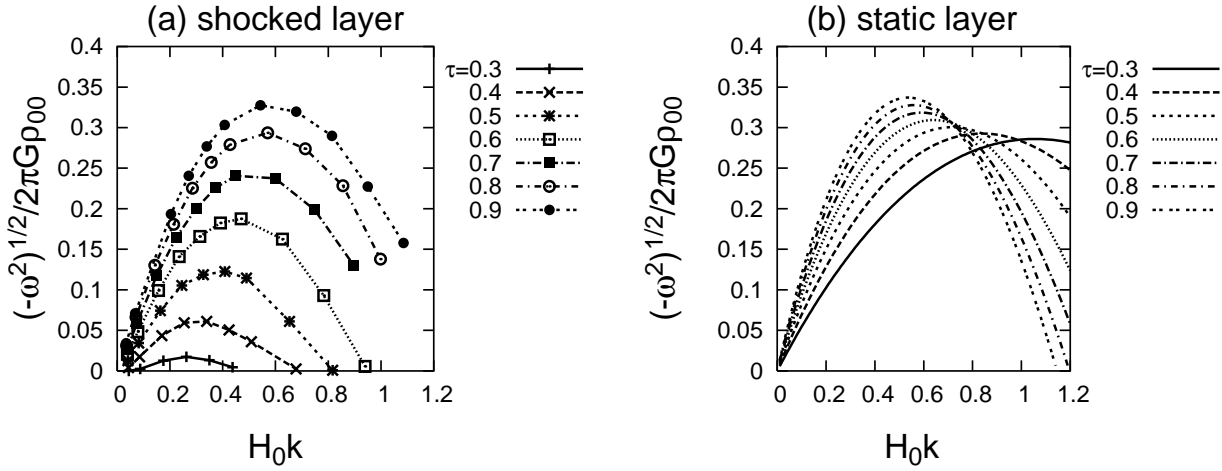


Fig. 9. (a) Dispersion relations derived from our calculation at each epoch for $\mathcal{M}=30$. (b) Dispersion relations of a static isothermal layer with the column density and an external pressure at each epoch (see GL65). The abscissa and the ordinate are normalized by the scale height H_0 and $2\pi G\rho_0$, respectively.

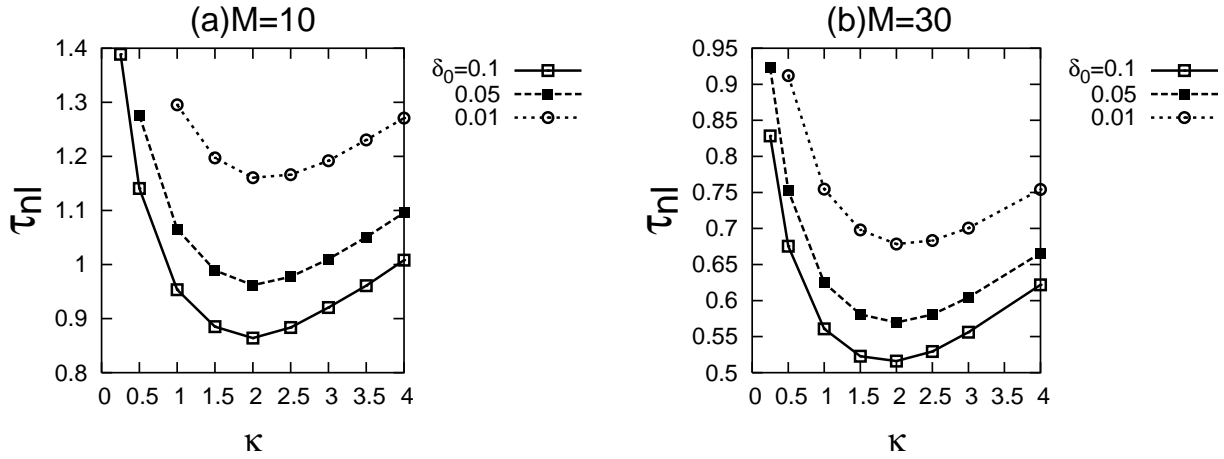


Fig. 10. Non-linear time defined by equation (37) for wavenumbers and initial amplitude for the case with $\mathcal{M}=(a)10$, (b)30

we neglect factors of order unity, τ_{nl} becomes $\sim \mathcal{M}^{-1/2}$. Therefore, $t_{nl} = \tau_{nl}/\sqrt{2\pi G\rho_E} \sim t_{ff}^{cloud}/\sqrt{\mathcal{M}}$ is inversely proportional to the growth rate at $t_{c,\kappa}$, where $t_{ff}^{cloud} = 1/\sqrt{2\pi G\rho_E}$. Note that t_{nl} is shorter than the free-fall timescale of the preshock region $\sim t_{ff}^{cloud}$ and larger than the free-fall timescale of the layer $t_{ff}^{layer} \sim t_{ff}^{cloud}/\mathcal{M}$. For larger Mach numbers, the difference among t_{nl} , t_{ff}^{cloud} and t_{ff}^{layer} becomes large. The origin of dependence $t_{nl} \propto 1/\sqrt{\mathcal{M}}$ is explained in subsection 2.2. In summary, $\kappa_{nl}=2$ and equation (38) are one of the main results in our linear analysis and that provide fragmentation length and time scales.

6. Discussion

6.1. Astrophysical Implications

As an application of equation (38), we seek criteria for collision-induced fragmentation. As a simplest case, we consider a spherical cloud with uniform density ρ_E , the mass M and radius R . This cloud is specified by one parameter, α_0 , which is defined by

$$\alpha_0 = \frac{U_o}{|W_o|} = \frac{5}{2} \frac{c_s^2 R}{GM}, \quad (39)$$

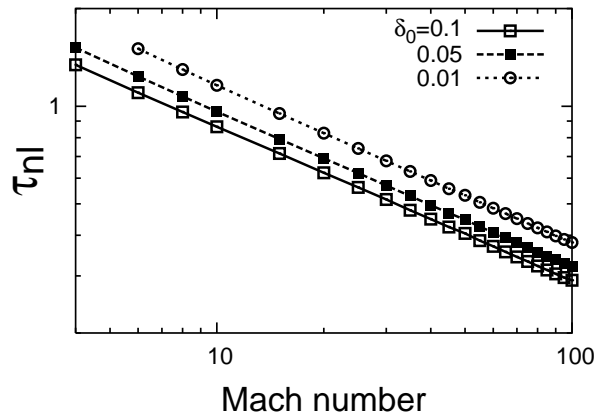


Fig. 11. Dependence of τ_{nl} on Mach numbers for the case with $\kappa=2$. Initial amplitude $\delta_0=0.01, 0.05$, and 0.1 are defined in equation (37)

where W_0 and U_0 are the gravitational and thermal energy of the cloud at the initial state, respectively. From equation (39) and $M \simeq 4\pi\rho_E R^3/3$, the radius is given by

$$2R = \sqrt{\frac{15c_s^2}{2\pi G\rho_E\alpha_0}}. \quad (40)$$

We consider the collision of two physically identical clouds with velocity $\pm\mathcal{M}c_s$ relative to the center of mass.

Fragmentation during cloud collision is expected if the following two conditions are satisfied (hereafter we adopt t_{nl} as fragmentation time).

1. $\tau_{\text{nl}} \lesssim \tau_{\text{conti}}$ The first condition is that fragmentation time, τ_{nl} , is shorter than the normalized collision continuous time, τ_{conti} , which is defined by

$$\tau_{\text{conti}} = \frac{2R}{\mathcal{M}c_s} \sqrt{2\pi G\rho_E}. \quad (41)$$

From equation (40) and (41), we obtain

$$\tau_{\text{conti}} \simeq \sqrt{15}\alpha_0^{-1/2}\mathcal{M}^{-1}. \quad (42)$$

Substituting equation (42) and our result of linear analysis [equation (38)] into $\tau_{\text{nl}} \lesssim \tau_{\text{conti}}$, the first condition for fragmentation is written as

$$\alpha_0 \lesssim 2.6\delta_0^{0.2}\mathcal{M}^{-1}. \quad (43)$$

2. $2c_s t_{\text{conti}} \lesssim 2R - \lambda_{\text{nl}}$ In order to assume the compressed region between two clouds as a layer, rarefaction wave from the cloud surface must not erode in an unstable region with λ_{nl} , which is given by

$$\lambda_{\text{nl}} = \frac{2\pi}{k_{\text{nl}}} \simeq 2\pi \frac{c_s}{2\sqrt{2\pi G\rho_E}\mathcal{M}}. \quad (44)$$

This condition is expressed as $2c_s t_{\text{conti}} \lesssim 2R - \lambda_{\text{nl}}$. With equation (40), (42) and (44), the above condition is rewritten as

$$\alpha_0 \lesssim \frac{15}{\pi^2}\mathcal{M} \left(1 - \frac{2}{\mathcal{M}}\right)^2. \quad (45)$$

Therefore, two conditions, (43) and (45), provide fragmentation criteria on α_0 and \mathcal{M} .

Figure 12 represents the two conditions on the (α_0, \mathcal{M}) plane. Fragmentation is expected in the dotted region. Figure 12 indicates that the case with $\alpha_0 \simeq 1$ can not be expected to fragment in all Mach numbers. This means that the collision of clouds in dynamical equilibrium does not induce fragmentation. By collision between clouds, only the case with small α_0 is expected to fragment the layer. In other words, only clouds with mass much larger than Jeans mass will fragment by cloud collision as long as isothermal.

If $\alpha_0 \lesssim 1$, each cloud collapses due to self-gravity. The collapse timescale is $t_{\text{dyn}} = \sqrt{3\pi/(32G\rho_E)}$, or $\tau_{\text{dyn}} = \sqrt{3}\pi/4$. The critical Mach number, \mathcal{M}_{eq} , in which τ_{nl} equals to τ_{dyn} , is given by

$$\mathcal{M}_{\text{eq}} \sim 3.1\delta_0^{-0.2}. \quad (46)$$

In Figure 12, thick dotted vertical line represents $\mathcal{M} = \mathcal{M}_{\text{eq}}$. In the region with $\mathcal{M} \lesssim \mathcal{M}_{\text{eq}}$ ($t_{\text{nl}} \gtrsim t_{\text{dyn}}$), the dynamical collapse of each cloud can not be ignored during fragmentation. Since our linear analysis does not include collapse of each cloud, a non-linear multi-dimensional calculation is required for further an investigation. In the region with $\mathcal{M} \gtrsim \mathcal{M}_{\text{eq}}$ ($t_{\text{nl}} \lesssim t_{\text{dyn}}$), the layer is expected to fragment before an individual collapse.

Nagasawa & Miyama (1987) investigated collisions between self-gravitating isothermal equilibrium spheres supported by an external pressure using three-dimensional calculations. They calculated cases by coalescence between two clouds with $\alpha_0 \sim o(1)$ and $\mathcal{M} \lesssim 10$. As a result, they found that a single cloud forms and it becomes gravitationally unstable. However, it does not fragment, but collapses as a single object. Our results are consistent with their results in $\alpha_0 \sim o(1)$ and $\mathcal{M} \lesssim 10$. However, in order to compare our results and to discuss the fragmentation process of the layer which is formed by a collision between clouds with $\alpha_0 < 1$, a much higher numerical resolution than previous calculation is required.

Boyd & Whitworth (2005) investigated the evolution of an oblate spheroidal cloud formed by a shocked layer using a semi-analytic method. Their clouds correspond to the unit wavelength in our model, while they included the effect of detailed thermal evolution. A cloud smaller than $\sim c_s/\sqrt{2\pi G\rho_E\mathcal{M}}$ oscillate, and then collapse, while larger clouds collapse monotonically. Their results are consistent with ours.

Finally, we comment on two possibilities of fragmentation that is induced by cloud collision in an actual astrophysical environment. The first possibility is a collision between clouds with $\alpha_0 < 1$ ($M > M_J$). From figure 12, the timescale of collision-induced fragmentation is smaller than that of the collapse of each cloud if collision velocity is $\mathcal{M} \gtrsim \mathcal{M}_{\text{eq}} \sim 5$ [equation (46)]. Therefore sheet fragmentation becomes dominant process in such a case of cloud collision. The second possibility is that α_0 becomes effectively smaller than order of unity after formation of the layer. This will be realized if the postshock region becomes cooler than the preshock region by cooling, even in a collision between clouds with $\alpha_0 \sim 1$.

7. Summary

We investigated the gravitational instability of isothermal layers bounded by shock waves. The results of our investigation are summarized as follows.

1. By imposing the shock boundary condition, the shocked layer is more stabilized than static layer, which is bounded by a constant external pressure. The stabilization influences the fragmentation process of the shocked layer.
2. In our linear analysis, the epoch at which the perturbations change from the oscillatory mode to the growing mode is well approximated by $t_{c,\kappa}$ [see equation (6)] derived from the 1-zone model.
3. Our unsteady linear analysis can provide the correct

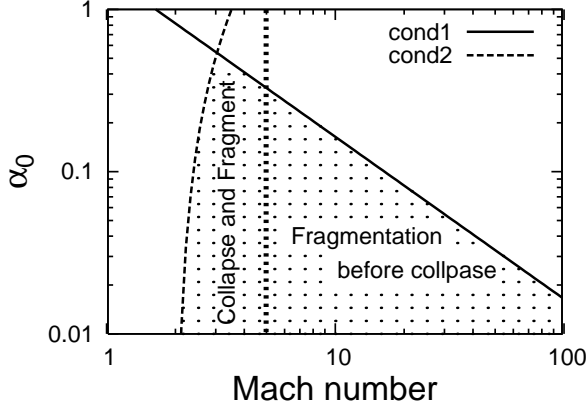


Fig. 12. Criterion of fragmentation. The solid and long-dashed lines correspond to $\tau_{\text{nl}} = \tau_{\text{cont1}}$ and $2c_s t_{\text{cont1}} = 2R - \lambda_{\text{nl}}$, respectively. The fragmentation region is shown to be in the dotted region. The short-dashed line represents $\tau_{\text{nl}} = \tau_{\text{dyn}} (\mathcal{M} = \mathcal{M}_{\text{eq}})$. The region with $\tau_{\text{nl}} > \tau_{\text{dyn}} (\mathcal{M} < \mathcal{M}_{\text{eq}})$ shows that the layer probably fragments during individual collapse. The region with $\tau_{\text{nl}} < \tau_{\text{dyn}} (\mathcal{M} > \mathcal{M}_{\text{eq}})$ shows that the layer can fragment before individual collapse.

fastest growing mode, which becomes non-linear at the earliest epoch. The wavenumber of the fastest growing mode is $k_{\text{nl}} = 2\sqrt{2\pi G \rho_E \mathcal{M}}/c_s$ ($\kappa_{\text{nl}} = 2$). This value, $\kappa_{\text{nl}} = 2$, is twice as large as the wavenumber, $\kappa = 1$, which begins to grow at the earliest epoch. The time at which this mode becomes non-linear is given by $t_{\text{nl}} = 2.4\delta_0^{-0.1}/\sqrt{2\pi G \rho_E \mathcal{M}}$.

4. Collision-induced fragmentation is expected only when $\alpha_0 = 5c_s^2 R/2GM$ of the parent clouds is much smaller than 1 (figure 12). In the collision between clouds with $\alpha_0 < 1$ and $\mathcal{M} \gtrsim 5$, the layer will fragment before individual collapse by self-gravity.

Acknowledgements

We thank Fumio Takahara and Yutaka Fujita for useful discussion and continuous encouragement. This work is in part supported by the 21st Century COE Program "Towards a New Basic Science; Depth and Synthesis" in Osaka University, funded by the Ministry of Education, Science, Sports and Culture of Japan.

Appendix 1. The Shock Boundary Conditions

A.1.1. Unperturbed Shock Boundary Conditions

In the rest frame of the postshock, we derive jump conditions of isothermal shock without self-gravity. A schematic picture is represented in figure 13. The physical variables in the preshock and the postshock regions are denoted by subscripts of "E" and "sh", respectively.

To begin, jump conditions in the unperturbed state are considered. From mass and momentum conservation across the shock front and the isothermal condition, we can derive the following equations:

$$\rho_{\text{sh}}(-\dot{z}_{\text{sh}}) = \rho_{\text{E}}(-V_{\text{E}} - \dot{z}_{\text{sh}}), \quad (\text{A1})$$

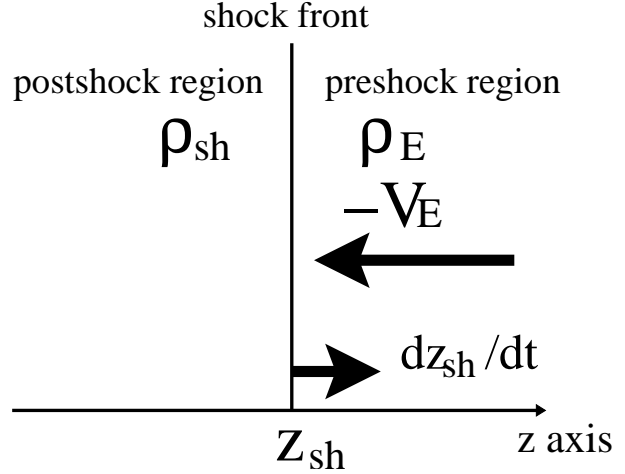


Fig. 13. Schematic picture of shock front in the rest frame of postshock.

$$P_{\text{sh}} + \rho_{\text{sh}}(-\dot{z}_{\text{sh}})^2 = P_{\text{E}} + \rho_{\text{E}}(-V_{\text{E}} - \dot{z}_{\text{sh}})^2, \quad (\text{A2})$$

and

$$\frac{P_{\text{sh}}}{\rho_{\text{sh}}} = \frac{P_{\text{E}}}{\rho_{\text{E}}} = c_s^2. \quad (\text{A3})$$

We define the flow velocity V_{sh} in the rest frame of the shock front by $V_{\text{sh}} = V_{\text{E}} + \dot{z}_{\text{sh}}$. Hence, by solving equations (A1), (A2) and (A3), we obtain

$$\rho_{\text{sh}} = \rho_{\text{E}} \mathcal{M}^2, \quad (\text{A4})$$

$$\dot{z}_{\text{sh}} = \frac{c_s}{\mathcal{M}}, \quad (\text{A5})$$

and

$$V_{\text{E}} = \left(\mathcal{M} - \frac{1}{\mathcal{M}} \right) c_s. \quad (\text{A6})$$

A.1.2. Perturbed Shock Boundary Conditions

Linearized jump conditions are derived. The position of the shock front is defined by $z_{\text{sh}}(x, t) = z_{\text{sh},0}(t) + \delta z_{\text{sh}}(t)e^{ikx}$. Linearized mass and momentum conservation across the shock front are given by

$$D\rho_{\text{sh}}(-\dot{z}_{\text{sh}}) + \rho_{\text{sh},0}(Dv_{z,\text{sh}} - \delta\dot{z}_{\text{sh}}) = -\rho_{\text{E}}\delta\dot{z}_{\text{sh}}, \quad (\text{A7})$$

and

$$D\rho_{\text{sh}}(c_s^2 + \dot{z}_{\text{sh}}^2) - 2\rho_{\text{sh},0}\dot{z}_{\text{sh}}(Dv_{z,\text{sh}} - \delta\dot{z}_{\text{sh}}) = 2\rho_{\text{E}}V_{\text{sh}}\delta\dot{z}_{\text{sh}}, \quad (\text{A8})$$

where operator "D" represents Lagrangian displacement. From equations (A7) and (A8), we have

$$D\rho_{\text{sh}} = 2\rho_{\text{E}} \frac{\mathcal{M}}{c_s} \frac{d\delta z_{\text{sh}}}{dt}, \quad (\text{A9})$$

and

$$Dv_{z,\text{sh}} = \left(1 + \frac{1}{\mathcal{M}^2} \right) \frac{d\delta z_{\text{sh}}}{dt}. \quad (\text{A10})$$

The relationship between the Lagrangian and Eulerian displacement is given by

$$D\rho_{\text{sh}} = D\rho_{\text{sh}}(z_{\text{sh},0} + \delta z_{\text{sh}}) = \delta\rho_{\text{sh}} + \delta z_{\text{sh}} \left(\frac{\partial \rho_0}{\partial z} \right)_{z_{\text{sh},0}}. \quad (\text{A11})$$

Next, we consider the velocity perturbation in the x -direction $\delta v_{x,\text{sh}}$. Momentum conservation for the tangential direction of the shock front gives

$$\delta v_{x,\text{sh}} = -V_E \frac{\partial \delta z_{\text{sh}}}{\partial x} = -ikV_E \delta z_{\text{sh}}. \quad (\text{A12})$$

We adopt the same boundary condition of the gravitational potential perturbation as in Welter (1982),

$$\frac{\partial \delta \phi_{\text{sh}}}{\partial z} + k\delta \phi_{\text{sh}} + 4\pi G(\rho_{\text{sh}} - \rho_E) = 0. \quad (\text{A13})$$

Appendix 2. Dispersion Relation of a Shocked Layer under 1-zone Model

The averaged physical quantities are defined by

$$\Sigma = \int_{-z_{\text{sh}}}^{z_{\text{sh}}} \rho dz \quad \text{and} \quad J_x = \int_{-z_{\text{sh}}}^{z_{\text{sh}}} \rho v_x dz. \quad (\text{A14})$$

The 0th-order equation is given by

$$\partial_t \Sigma_0 = \rho_E V_{\text{sh}}, \quad (\text{A15})$$

where the subscript "0" represents the unperturbed variable and differential operators $\partial/\partial t$ and $\partial/\partial x$ are abbreviated by ∂_t and ∂_x , respectively. Let us consider the perturbation variables $\delta\Sigma$, δJ_x and δL , which are defined by

$$\Sigma(x, t) = \Sigma_0(t) + \delta\Sigma(x, t), \quad (\text{A16})$$

$$J_x(x, t) = \delta J_x(x, t), \quad (\text{A17})$$

and

$$L(x, t) = L_0(t) + \delta L(x, t), \quad L(x, t) = 2z_{\text{sh}}(x, t). \quad (\text{A18})$$

The column density perturbation, $\delta\Sigma$, can be divided into two contributions, as follows:

$$\delta\Sigma = \rho_{\text{sh}} \delta L + \delta\sigma, \quad \text{where} \quad \delta\sigma = \int_{-z_{\text{sh},0}}^{z_{\text{sh},0}} \delta\rho dz. \quad (\text{A19})$$

The linearized equation of mass conservation is given by

$$\partial_t \delta\Sigma = \rho_E \partial_t \delta L - \partial_x \delta J_x \sim -\partial_x \delta J_x. \quad (\text{A20})$$

Since $\delta\Sigma \sim \rho_{\text{sh}} \delta L \gg \rho_E \delta L$, linearized equation of momentum conservation in the x -direction is given by

$$\begin{aligned} \partial_t \delta J_x &= \rho_E V_{\text{sh}} (-V_E \partial_x \delta L) - c_s^2 \partial_x \delta\sigma + 2\pi G \Sigma_0 \partial_x \delta\Sigma / k \\ &\sim -\rho_E \mathcal{M}^2 \partial_x \delta L - c_s^2 \partial_x \delta\sigma + 2\pi G \Sigma_0 \partial_x \delta\Sigma / k. \\ &= -c_s^2 \partial_x \delta\Sigma + 2\pi G \Sigma_0 \partial_x \delta\Sigma / k. \end{aligned} \quad (\text{A21})$$

The second term in the first line of the equation (A21) represents the momentum flux as a result of the shock boundary condition. The second line of the equation (A21) is derived using $V_E \sim \mathcal{M} c_s$. The third line is derived by using $\rho_{\text{sh}} = \rho_E \mathcal{M}^2$ and equation (A19).

Neglecting the time-dependence of $\Sigma_0(t)$, from equation (A20) and (A21), the approximate dispersion relation is derived as

$$\omega^2 \sim c_s^2 k^2 - 2\pi G k \Sigma_0(t). \quad (\text{A22})$$

Appendix 3. A Layer Confined by Constant External Pressure

We investigate a highly compressed static layer that is mainly confined by constant external pressure, P_b . In this situation, the layer has almost uniform density, denoted by ρ_0 . The momentum conservation equation in x -direction is given by

$$\partial_t \delta J_x = -c_s^2 \partial_x \delta\sigma + 2\pi G \Sigma_0 \partial_x \delta\Sigma / k, \quad (\text{A23})$$

where the second term of first line of equation (A21) is absent due to the constant pressure boundary conditions. Because the layer is very thin, $\delta\rho$ is approximately determined only by boundary value of $\delta\rho$ as $\delta\sigma \simeq \delta\rho(z = z_b) L_0$, where z_b is the position at the boundary of the layer. The constant pressure boundary condition is given by

$$D\rho = \delta\rho(z_{b,0}) + \delta z_b (\partial_z \rho_0)_{z_{b,0}} = 0, \quad (\text{A24})$$

(see GL65). Because the unperturbed state is hydrostatic equilibrium, $(\partial_z \rho_0)_{z_b} = -\rho_0 (\partial_z \phi_0)_{z_b} / c_s^2 = -2\pi G \rho_0^2 L_0 / c_s^2$. Therefore, the ratio of $\delta\sigma$ to $\rho_0 \delta L$ is written as

$$\delta\sigma / \rho_0 \delta L \sim (L_0 / H_0)^2 \ll 1. \quad (\text{A25})$$

From $\delta\Sigma \sim \rho_0 \delta L$ and equation (A25), the second term of the equation (A23) becomes

$$-c_s^2 \partial_x \delta\sigma \sim -c_s^2 \left(\frac{L_0}{H_0} \right)^2 \partial_x \delta\Sigma. \quad (\text{A26})$$

Thus, the pressure term is $\sim (L_0 / H_0)^2$ times as small as that of the shocked layer [equation (3)]. Moreover, $c_s(L_0 / H_0)$ is rewritten with equation (7) as

$$c_s \left(\frac{L_0}{H_0} \right) \sim \sqrt{g_0 L_0}, \quad g_0 \equiv 2\pi G \rho_{00} L_0 \sim 2\pi G \Sigma_0, \quad (\text{A27})$$

where $\Sigma_0 \simeq \rho_{00} L_0$. This corresponds to the phase velocity of gravity wave in shallow water. Finally, the dispersion relation is given by

$$\omega^2 \sim \left(\frac{L_0}{H_0} \right)^2 c_s^2 k^2 - 2\pi G k \Sigma_0 \sim 2\pi G \Sigma_0 (L_0 k^2 - k) \quad (\text{A28})$$

From equation (A28), $(\sqrt{-\omega^2})_{\text{max}}$ is almost the free-fall growth rate of the layer and λ_{max} is nearly equal to the thickness $\sim L_0$. The smaller scale perturbation can grow much faster than in the shocked layer because the pressure effect is small.

From the above simple analysis, we understand the following things. For $(L_0 / H_0) \simeq 1$, the difference of boundary condition does not influence on the evolution of the perturbations, and the dispersion relations become the same form as equation (A22). However, for $(L_0 / H_0)^2 \ll 1$, the constant-pressure boundary condition is in completely different from that of the shock boundary condition.

Appendix 4. Validity of Approximation ($v_{z,0} = 0$)

The validity of the approximation $v_{z,0} = 0$ is considered in this section. The perturbation equations containing $v_{z,0}$ are given by

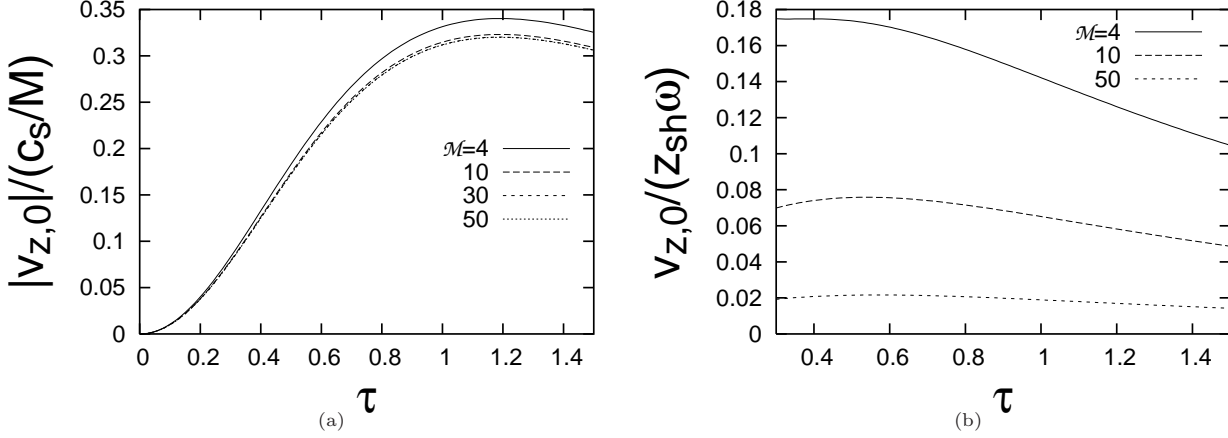


Fig. 14. (a): Analytic expression (A32) is shown for $\mathcal{M} = 4, 10, 30, 50$. (b): Plots of $v_{z,0}/(z_{sh}\omega)$. Each variable is from equation (A32)($v_{z,0}$), equation (3)(ω) and equation (11)(z_{sh}).

$$\frac{\partial \delta \rho}{\partial t} + \frac{\partial}{\partial z}(\rho_0 \delta v_z + \delta \rho v_{z,0}) = -ik\rho_0 \delta v_x, \quad (\text{A29})$$

$$\begin{aligned} \frac{\partial}{\partial t}(\rho_0 \delta v_z + \delta \rho v_{z,0}) + \frac{\partial}{\partial z}(c_s^2 \delta \rho + 2\rho_0 v_{z,0} \delta v_z + \delta \rho v_{z,0}^2) \\ = -ik\rho_0 v_{z,0} \delta v_x - \delta \rho \frac{\partial \phi_0}{\partial z} - \rho_0 \frac{\partial \delta \phi}{\partial z}, \end{aligned} \quad (\text{A30})$$

and

$$\frac{\partial}{\partial t}(\rho_0 \delta v_x) + \frac{\partial}{\partial z}(\rho_0 v_{z,0} \delta v_x) = -ikc_s^2 \delta \rho - ik\rho_0 \delta \phi. \quad (\text{A31})$$

For $|z| < |z_{sh}|$, the velocity $|v_{z,0}(z)|$ is smaller than $|v_{z,0}(z_{sh})|$ at shock front. If we assume that the shock front position is given by equation (11), we can express $v_{z,0}(z_{sh})$ approximately from the jump conditions

$$v_{z,0}(z_{sh}) = -\frac{c_s}{\mathcal{M}} \left(\frac{1}{1 - f(\tau)/\mathcal{M}^2} + f(\tau) - 1 \right), \quad (\text{A32})$$

where f is given by

$$f(\tau) = \tau \cosh^{-1} \sqrt{1 + \tau^2} / (1 + \tau)^{3/2}. \quad (\text{A33})$$

Figure 14a shows the time evolution of $|v_{z,0}(z_{sh})|$ for various Mach numbers. This figure indicates that the maximum value of $|v_{z,0}(z_{sh})|$ is slightly less than, or comparable to, $\sim 0.3c_s/\mathcal{M}$. The average velocity, $|\bar{v}_{z,0}|$, of the layer is clearly smaller than this value.

Let us consider the contribution of $v_{z,0}(z_{sh})$ for the perturbation equations. To begin with, we compare the two terms $\delta \rho v_{z,0}$ and $\rho_0 \delta v_z$ in perturbed momentum in the z -direction. The ratio of the two terms is given by $(\delta \rho v_{z,0})/(\rho_0 \delta v_z) < 0.3c_s(\delta \rho/\delta v_{z,0})/\mathcal{M}^3 \ll 1$; thus, we can approximate the perturbed momentum in the z -direction as $\rho_0 \delta v_z$. Therefore, we can neglect the third term of equation (A29) and the second term of equation (A30). Moreover, we can neglect the fifth term of equation (A30), which is smaller than the third term by $0.3/\mathcal{M}^2$. In equation (A30), the ratio of the fourth to the first terms is given by $\sim v_{z,0}/(L_0\omega)$. This ratio is small value if Mach number is large (see figure 14b). For the same reason, we

can neglect the second term of equation (A31) compared with the first term. The ratio of the sixth term of equation (A30) to the first term is given by $(k/\omega)v_{z,0}(\delta v_x/\delta v_z) \lesssim (0.3/\mathcal{M})(\delta v_x/\delta v_z)$. This value is also small if the Mach number is large. From the above discussion, $v_{z,0}$ can be assume to be zero.

References

- Ashman, K.M. & Zepf, S. 1992 *ApJ*, 384, 50
 Blaauw, A. 1964 *ARA&A*, 2, 213
 Boyd, D.F.A., & Whitworth, A.P., 2005 *A&A*, 430, 1059
 Elmegreen, B.G., & Elmegreen, D.M. 1978 *ApJ*, 220, 1051
 Elmegreen, B.G., & Lada, C.J. 1977 *ApJ*, 214, 725
 Fujimoto, M., & Noguchi, M. 1990 *PASJ*, 42, 505
 Goldreich, P., & Lynden-Bell, D. 1965 *MNRAS*, 130, 97
 Hasegawa, T., Sato, F., Whiteoak, J.B. & Miyawaki, R. 1994 *ApJ*, 429, L77
 Herbst, W. & Assousa, G.E. 1977 *ApJ*, 217, 473
 Hubbard, M.E., & Garcia-Navarro, P. 2000 *J. Comput. Phys.* 165, 89
 Kumai, Y., Basu, B., & Fujimoto, M. 1993 *ApJ*, 404, 144
 Nagasawa, M., & Miyama, S.M. 1987 *Prog. Theor. Phys.*, 78, 1250
 Sato, F., Hasegawa, T., Whiteoak, J.B., & Miyawaki, R. 2000 *ApJ*, 535, 857
 Vishniac, E.T. 1994 *ApJ*, 428, 186
 Welter, G.L. 1982 *A&A*, 105, 237
 Whitworth, A.P., Bhattal, A.S., Chapman, S.J., Disney, M.J., & Turner, J.A. 1994 *A&A*, 290, 421